Numerical modelling of glulam frames with buckling restrained braces

Wenchen Dong, Minghao Li, Chin-Long Lee, and Gregory MacRae

Department of Civil and Natural Resources Engineering, University of Canterbury, New Zealand

Abstract

This paper presents a component-based numerical model to simulate seismic behaviour of a timber-steel hybrid structure consisting of glulam frames braced by buckling restrained braces (BRBs). The model is validated by existing experimental data of two full-scale BRB-braced glulam frames (BRBGFs) where dowelled connections and screwed connections were used as the critical BRB-timber interface connections, respectively. Parametric studies are also conducted by the validated model to investigate the influence of the interface connection stiffness and manufacturing tolerances on the performance of the BRBGFs. The studies showed that the interface connection overstrength factor γ = 1.5 was a suitable value to engage BRBs, ensure ductile behaviour and achieve a cost-effective connection design. Manufacturing tolerances had a negligible impact on the ultimate strength and energy dissipation under cyclic loading but might affect the performance under serviceability limit state loads.

Keywords: buckling restrained braces (BRBs); glulam frames; dowelled connections; screwed connections; numerical modelling

1 Introduction

Multi-storey timber buildings are becoming popular around the world with the rapid development of high-performance engineered wood products [1] as well as the sustainability driver in the building industry. However, timber has a relatively lower elastic modulus compared with other construction materials. Larger member sizes are often needed for multi-storey timber buildings to satisfy stiffness requirements. In heavy timber frames, beam-column connections are mostly designed to only transmit shear loads. This is because the rotational stiffness of timber connections is relatively low and the shear connections under moment have a possibility of brittle failure in the perpendicular-to-grain direction [2]. Additional braces or shear walls are often needed to form lateral force resisting systems (LFRS) in heavy timber frames. In countries with a high seismic risk like New Zealand, seismic considerations usually govern the design of LFRS of multi-storey buildings [3,4].

In conventional braced timber frames, energy dissipation under seismic loads is designed to concentrate on the end connections of the timber braces because timber braces are brittle in tension [5]. These connections can be damaged severely during major earthquakes, which makes the repair difficult. In addition, force-drift hysteresis curves of conventional braced timber frames show pronounced pinching effects with strength and stiffness degradation. Due to these limitations, the performance of conventional braced timber frames may lead to uneconomical member design or limit the building height [6]. In this regard, LFRS that provides better performance may facilitate the design of multi-storey timber buildings in high seismic zones [7,8].

In efforts to provide improved seismic performance, two full-scale buckling restrained braces (BRBs) braced glulam frames (BRBGFs) were designed and tested by the authors [9]. It was shown that replacing the conventional timber braces with BRBs significantly increased the energy dissipation capacity, minimized the damage in the connections, and potentially improved the reparability after severe earthquakes. Nevertheless, large-scale structural testing is expensive and time-consuming, allowing studies of only a very limited number of design configurations. A robust numerical model is needed to provide a more comprehensive understanding of the structural behaviour. Various numerical models for BRBs and BRB frames (BRBFs) with different connection details were established for steel structures [10–18] and reinforced concrete (RC) structures [19,20]. The numerical results showed that the BRBF performance can be represented well by the BRB models and connection assumptions.

The numerical studies of BRBGFs have also been conducted before [21,22], but the BRB-timber interface connections were simply simulated as pinned connections without considering the flexibility and the potential initial slips of the BRB-timber interface connections. The numerical studies also indicated that the performance of BRBGFs were good if appropriate connection design details were provided. The critical BRB-timber interface connections need to be verified by experimental tests and modelled in detail to achieve more accurate prediction of the performance of BRBGFs.

In the BRBGF tests [4], dowelled connections and screwed connections were used to connect BRBs with the glulam frames, respectively. The strength and stiffness of dowel-type connections can be calculated by design standards such as Eurocode 5 [23]. Past research on various types of dowel-type connections [24–27] showed that Eurocode 5 conservatively predicted the strength of dowel-type connections. However, the stiffness prediction equation in Eurocode 5, shown in Eq. 1, often considerably overestimates the connection stiffness [27–

29]. This may be because Eq. 1 is based on simplified assumptions without considering important influencing parameters such as fastener slenderness and quantity [30]. Jockwer and Jorissen [30] also showed that stiffness equations among different standards are quite different. None of them provides an accurate stiffness prediction for connections with multiple dowels and inserted steel plates. To improve the stiffness prediction accuracy, beam-on-foundation (BOF) models based on simple embedment tests were proposed for timber-to-timber dowel-type connections [31,32]. However, for steel-to-timber dowel-type connections such as those that connect BRBs to a timber frame, further investigation is required [32]. In addition, the dowel-type connections usually have lower initial stiffness caused by oversized holes for easy installation. The influence of the manufacturing tolerances on the overall performance is still unknown.

$$k_{ser,lat} = \lambda \rho_m^{1.5} \frac{d}{23} \qquad \text{Eq. 1}$$

where, $k_{ser,lat}$ (N/mm) is the lateral stiffness per shear plane per fastener under serviceability limit state (SLS) loads; $\lambda = 1$ and $\lambda = 2$ are the modification factor for timber-to-timber connection and timber-to-steel connection, respectively; ρ_m is the mean density of timber (kg/m^3); and d is the diameter of fastener (mm).

The strength of screwed connections using inclined self-tapping screws (STS) can also be calculated by Eurocode 5, and STS axial withdrawal stiffness calculations can follow European Technical Approvals (ETA) provided by screw suppliers. Eq. 2 and Eq. 3 from ETA 11/0190 [33] and ETA 11/0030 [34] are often used to estimate the STS axial withdrawal stiffness $k_{ser,ax,\theta}$ in softwood. However, these have been found to have errors up to 720% [35,36]. Alternatively, analytical models were proposed for stiffness predictions of inclined STS for timber-to-timber connections [37,38] and timber-to-concrete connections [39], but the feasibility of these analytical models for timber-to-steel connections still need to be verified.

$$k_{ser,ax,\theta,1} = 780 d^{0.2} l_{ef}^{0.4} \qquad \text{Eq. 2}$$

$$k_{ser,ax,\theta,2} = 25 d l_{ef} \qquad \text{Eq. 3}$$

where, $k_{ser,ax,\theta}$ (N/mm) is the axial stiffness per STS under SLS loads with an angle of θ to timber grain; d is the outer diameter of the STS (mm); l_{ef} is the penetration length in the timber member (mm).

According to the above discussion, there is a need to quantify the BRB-timber interface connection behaviour and to model the behaviour of BRBGFs. This study seeks to address this need by developing component models in OpenSees [40] for BRBs and connections. One-bay one-storey BRBGF numerical models will be validated by the full-scale BRBGF test data, and in particular, answers will be sought to the following questions:

1) Can stiffness of the dowelled and screwed connections in the BRBGFs be predicted by numerical models or analytical methods?
2) Can the overall performance of BRBGFs be represented by numerical models?
3) How does the stiffness of BRB-timber interface connections influence the BRBGF performance?
4) What is the effect of manufacturing tolerances on the BRBGF performance?

This research will focus on developing a robust component-based model that can well capture the behaviour of the critical BRB-steel interface connections and the system behaviour of BRBGFs. The model with reasonable computational efficiency and prediction accuracy will be used in parametric studies to investigate the key influence factors on the performance of BRBGFs and to facilitate the design of this hybrid system.

2 Numerical modelling

2.1 Components in BRBGFs

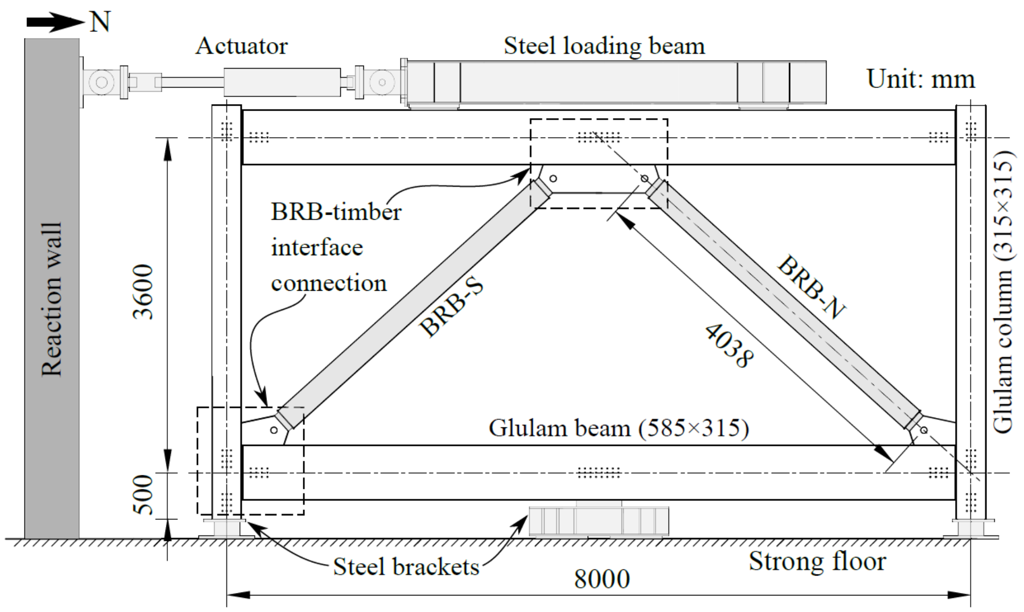

Figure 1 Specimen setup

Two 8 m wide and 3.6 m high BRBGFs, as shown in Figure 1, were tested by Dong et al. [4]. Figure 2 shows the BRB-timber interface connections at the middle span of beam used by the two BRBGF specimens, respectively. The specimens with the dowelled connections and screwed connections were denoted as S-D and S-S, respectively. In the dowelled connections, two steel plates were inserted into prefabricated slots in timber members, while in the screwed connections, steel plates were attached to the outside of the timber members. The BRBs were designed as ductile components while the glulam members and connections were protected by the capacity design to remain elastic before BRBs reached the maximum expected storey drift ratio, i.e. 2%. In addition, the BRB components were tested in accordance with AISC 341-16 [41]. Table 1 lists the properties of main components. The numerical model of the BRBGFs consisted of three main components: glulam members, BRBs and BRB-timber interface connections.

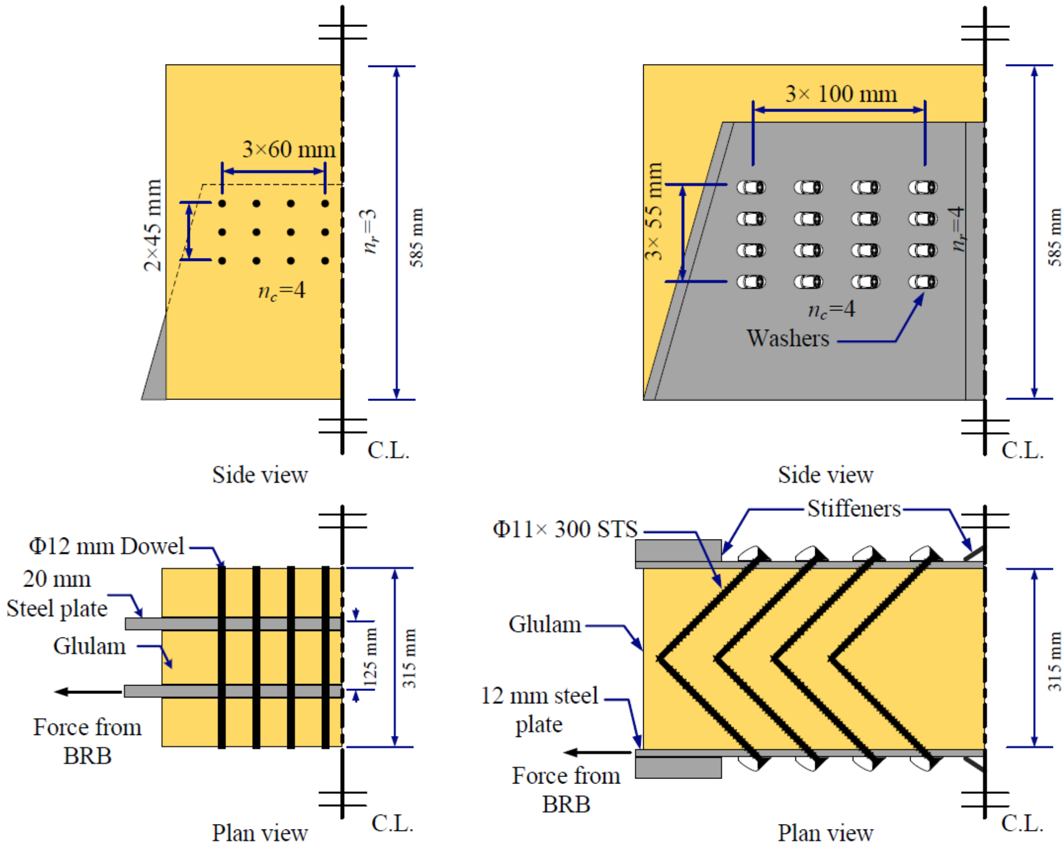

(a) Dowelled connection (b) Screwed connection

Figure 2 Connection details

Table 1 BRBGF components and properties

Specimen	Timber members	BRBs	Gusset plates	Fasteners
S-D	GL10 Radiata Pine [42] for beam (585 mm × 315 mm) and column (315 mm × 315 mm)	Core steel: 70 mm × 16 mm Q235 [43] flat plate	Two Grade 300 [44] 20 mm thick steel plates	Dowels: Φ12 mm Grade 300 round bars
S-S			Two Grade 350 [44] 12 mm thick steel plates with stiffeners	Inclined Screws: Φ11 × 300 mm STS [34] with inclined washers [45]

2.2 Modelling of BRB components

The *Steel4* material model in OpenSees has been successfully used previously to simulate BRB behaviour including asymmetric hardening [46]. Thus, the BRB component was represented by a truss element with this model and a cross section area of the steel core (A_c). Extra stiffness outside the steel core yield zone of BRBs, i.e. transition zone and elastic zone, was considered by a stiffness modification factor (f_{sm} = 1.22) for this BRB geometry as defined in Eq. 4 by Vigh et al. [13]. The BRB geometry was obtained from the experimental test data [9]. Because *Steel4* is highly customizable, overfitting becomes a potential issue [46] if limited BRB test data are used for parameter calibration. To avoid the overfitting issue, the BRB test calibration from Zsarnóczay and Vigh [47] was used except for the yield strength f_y and the isotropic hardening ratio b_{iso}, since these two parameters are determined by properties of the steel material [46]. An average f_y = 294MPa and b_{iso} = 0.08% were verified by steel coupon tests and the BRB component tests conducted in [9], respectively. More details about *Steel4* calibration parameters can be found in Appendix I and [47].

$$f_{sm} = \frac{l_{tot}}{l_c + l_{tr}\left(\frac{A_c}{\sqrt{A_{el}A_c}}\right) + l_{el}\frac{A_c}{A_{el}}} \qquad \text{Eq. 4}$$

where, l_{tot}, l_c, l_{tr}, and l_{el} are the total length, yield zone length of the steel core, transition zone length and elastic zone length of BRB (mm), respectively; A_c, A_{tr}, and A_{el} are the cross section area of yield zone of steel core, transition zone and elastic zone, respectively.

The BRB component tests showed higher strength, initial stiffness and post-yielding stiffness than the theoretical values [9]. There were several potential reasons for the higher strength and stiffness: 1) unbonding materials were stuck on the steel core tightly and transferred some loads to the concrete so the concrete worked as a spring parallel to the steel core [46,48]. 2) Due to the inappropriate casting of concrete, the spaces at both ends of BRBs were not sufficient, so the outward movement of steel core pushed concrete against the end cap plate as shown in Figure 3a, so the restraint from the end cap plate also worked as a spring parallel to the steel core. 3) The steel core was out of straightness during manufacturing, which required additional forces to straighten the steel core in tension. 4) The local buckling of steel core was initiated at the position close to the transition zone and the radius from the yield zone to the transition zone as shown in Figure 3b had an influence on the strength and stiffness on both tension and compression proved by Jones [49]. All of these provided extra restraints for the steel core.

The theoretical initial stiffness of the BRB $k_{BRB,theo}$ was 71 kN/mm using Eq. 5 and the post-yielding stiffness was expected to be below 2% of the initial stiffness [50]. However, test results showed the initial and post-yield stiffness were 98 kN/mm and 3 kN/mm, respectively. After yielding of the BRBs, the deformation was primarily concentrated on the local zone close to the transition zone as shown in Figure 3b, so the restraints were reduced. Because the reasons of additional restraints were complicated, more experimental tests and sensitivity analysis are needed to quantify the restraints more accurately as suggested by Jones [49], which is out of the scope of this paper. To consider the additional restraints provided to the steel core and to match experimental behaviour, an elastoplastic spring was added parallel to the BRB with calibrated initial stiffness of 27 kN/mm and post-yielding stiffness of 2.7 kN/mm as shown in Figure 4. The spring was modelled by *Steel01* material model and its yield displacement was the same as the BRB yielding displacement (4.6 mm) derived from the testing [9]. Figure 4 shows that the BRB component modelling results matched the experimental results well. The BRB specimen still showed slightly higher unloading stiffness in compression than the model. This was likely because the limited gaps between steel core and concrete grout restrained the steel core's transverse expansion under compression.

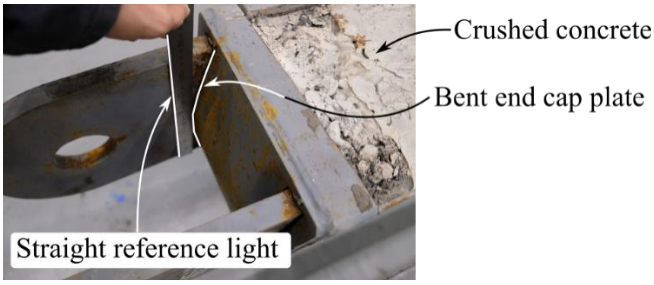

(a) End cap plate bending

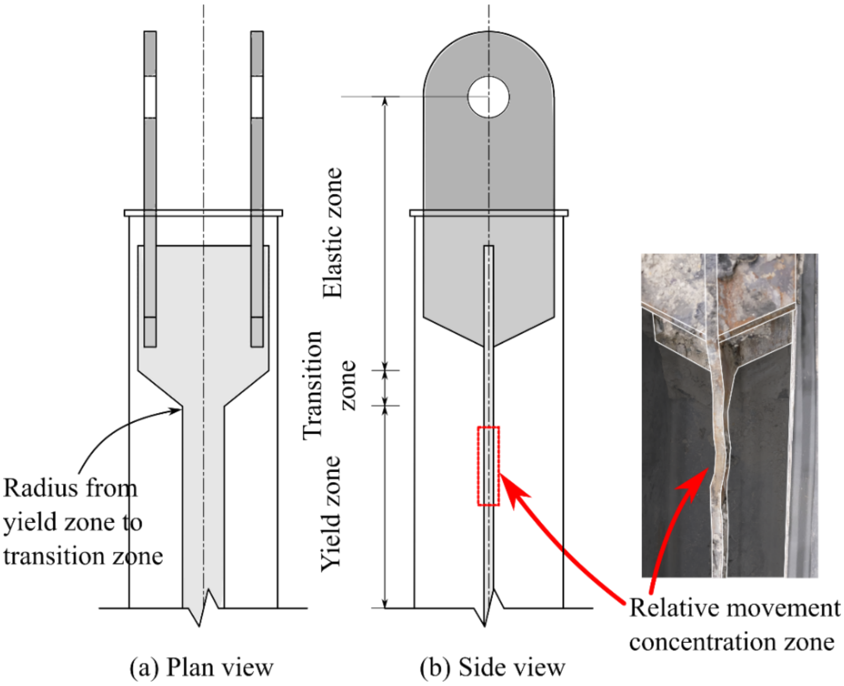

(b) BRB movement concentration

Figure 3 BRB movement observation

$$k_{BRB,theo} = \frac{E_{eq}A_c}{l_{tot}} = 71\ kN/mm \qquad \text{Eq. 5}$$

where, $k_{BRB,theo}$ is the theoretical axial stiffness of BRB (kN/mm), E_{eq} (= $f_{sm}E_s$) is the equivalent elastic modulus of BRB (GPa) by considering the additional stiffness outside the yield zone; E_s (= 206 GPa) is the elastic modulus of core steel; A_c is the core steel area (mm^2); l_{tot} (= 4038 mm) is the BRB pin-to-pin length.

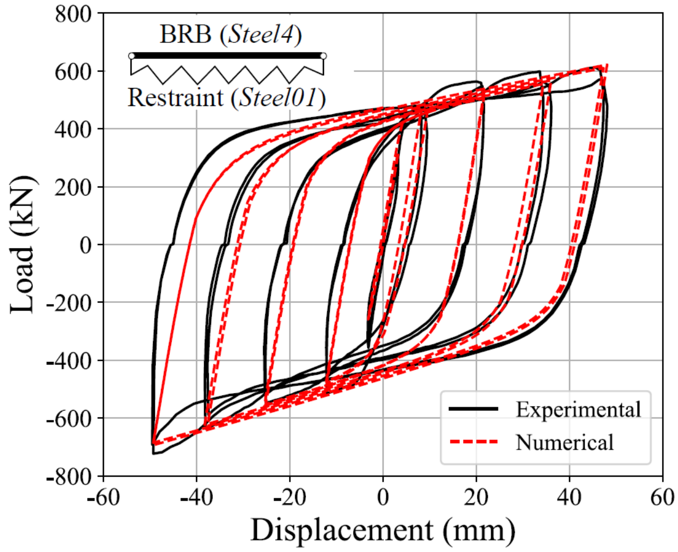

Figure 4 Comparison of BRB

2.3 Modelling of BRB-timber interface connections

2.3.1 Dowelled connections

The connection stiffness from tests was only 50% of predicted value by Eurocode 5 [9]. Therefore, the BOF methods proposed by Lemaitre et al. [32] was used to build the dowelled connection model in OpenSees. Figure 5 shows the model of dowelled connections and the parameters used in the BOF model are listed in Table 2. The timber members and steel plates were assumed to be elastic. Steel plates transferred the load to the dowels by steel bearing which was assumed to be rigid. All non-linearity was from dowel yielding and the timber embedment deformation. The dowels were modelled as elastoplastic beams and the timber embedment behaviour was modelled by a series of non-linear springs. The distance between springs was 4 mm (< 0.4*d*, where *d* is the dowel diameter) as suggested by Lemaitre et al. [32]. As shown in Figure 6, six glulam embedment tests were conducted in accordance with ASTM D5764 [51] to obtain the compressive load-displacement relationship between the dowel-timber interface. The average curve was used to calibrate the non-linear springs as shown in Figure 6b where the vertical coordinate is presented as the equivalent distributed load (N/mm) at unit length along the dowel. The force of each spring in Figure 5 will be the product of the equivalent distributed load and the distance between springs (i.e. 4 mm). The BOF modelling result was input as the backbone curve to model the cyclic response by *Pinching4* model in OpenSees and the model parameters can be found in the Appendix I.

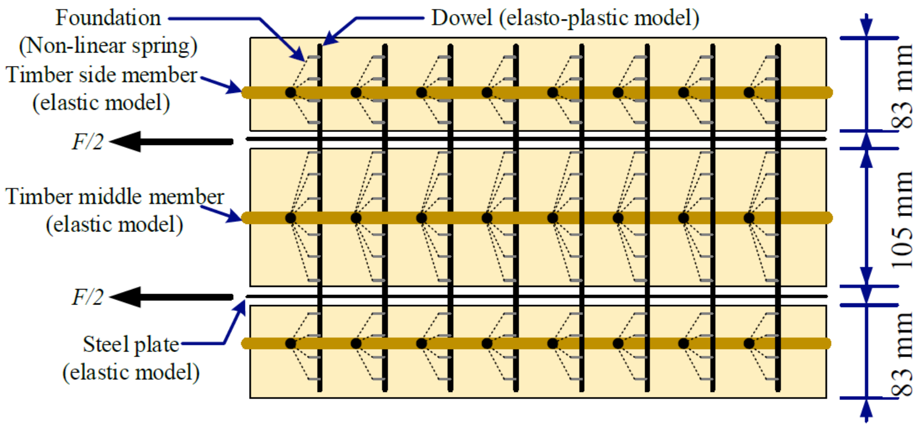

Figure 5 Plan view of BOF model for the dowelled connection

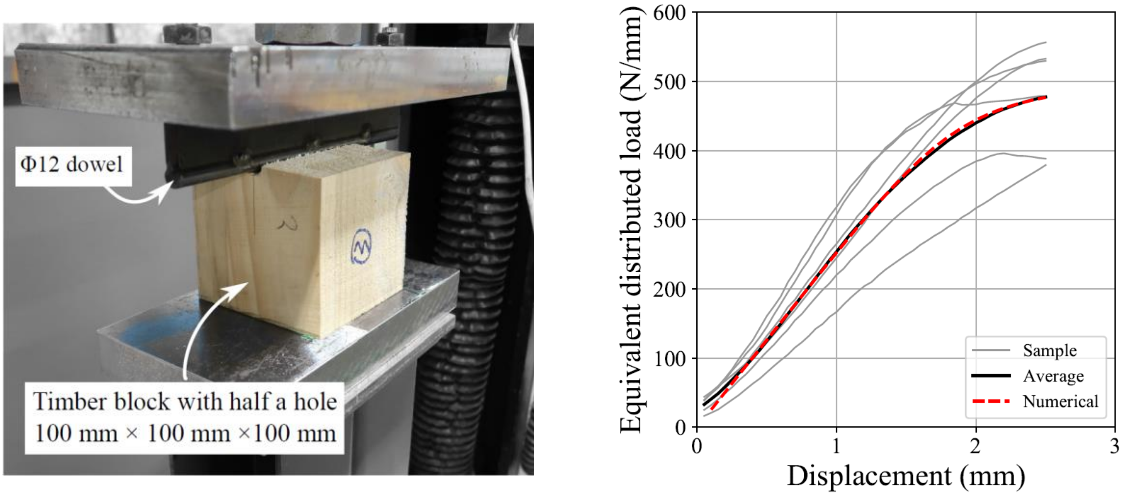

(a) Embedment test setup (b) Experimental and numerical results

Figure 6 Embedment tests and model calibration

Table 2 The BOF model parameters for the dowelled connection

Members	Element and materials	Parameters
Timber members	*elasticBeamColumn*	Side member: $A_s = 585\times83$ mm^2 $E_w = 10000$ MPa; Middle member: $A_m = 585\times105$ mm^2 $E_w = 10000$ MPa;
Steel plates	*elasticBeamColumn*	$A_{st} = 120\text{x}20$ mm$^{2;}$ $E_{st} = 210000$ MPa;
Steel-steel interface	*EqualDOF*	N/A
Dowels	*dispBeamColumn* with fibre cross section	f_{yd}=300 MPa; E_d= 210000 MPa; d= 12 mm;
Timber-steel interface	*ZeroLength* with *Steel02*	Element size= 4 mm f_{ts}=1964 N; E_{ts}=1012 N/mm b=0.01; R=6.0; r_1=0.925; r_2=0.15

Note: the parameter definition follows OpenSees documentations [40]

Because the holes in steel plates are larger than the dowels and the drilling causes surrounding area of the holes in timber members softer than other parts of timber [52], initial slips are typical in the dowelled connections. An additional spring with low initial stiffness within ±0.5 mm and very high stiffness beyond ±0.5 mm was simulated by *ElasticMultiLinear* model in OpenSees and placed in series with the *Pinching4* model to capture the actual connection response as shown in Figure 7. The range of ±0.5 mm was chosen since the diameter of the holes in the steel plate was 1 mm bigger than the dowels. The connection movement were measured by particle tracking technology (PTT), an advanced contact-free measurement technique in the BRBGF tests [9]. It was observed by Popovski [5] and from our BRBGF tests [9] that even under small displacements, there was some permanent bearing deformation and the unloading stiffness was higher than the initial stiffness. The unloading stiffness was considered as twice the initial stiffness based on the experimental observation from PTT. No strength degradation was considered in the model because the connections were not expected to be damaged. The simulation results were compared with the experimental results and Figure 7 shows that the model predicted the test results conservatively. This could be due to the asymmetry distribution of the gaps for each dowel. Some dowels might be engaged earlier on one side than the other. In addition, timber defects such as knots could also contribute to the asymmetric performance.

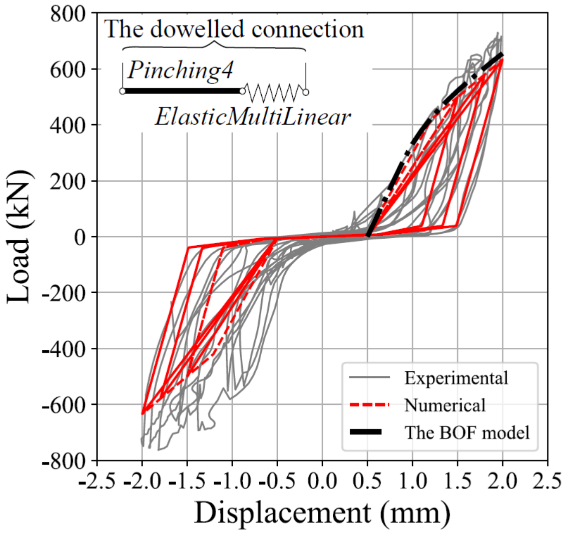

Figure 7 Comparison of the dowelled connection

2.3.2 Screwed connections

Eq. 6 from Tomasi et al. [37] with $k_{ser,ax,\theta,2}$ (Eq. 3) from ETA 11/0030 [34] considerably overestimated the actual stiffness of STS connections by 223% even without considering frictional effects [9]. One main reason could be that $k_{ser,ax,\theta,2}$ from ETA 11/0030 is not appropriate to estimate the axial stiffness $k_{ser,ax,\theta}$ for long STS [53]. Another reason could be that Eq. 6 does not consider the influence of STS flexibility caused by the free length (l_f highlighted in yellow colour in Figure 8) in the steel plate. The free length is due to the oversize of slotted holes in the steel plates and the lack of bearing (shank or thread) of STS on the steel plate. Tests of inclined STS with countersunk holes in the steel plate showed much higher stiffness [54], which proved the influence of l_f.

$$k_{ser,STS} = k_{ser,lat} sin\theta\left(sin\theta - \mu_f cos\theta\right) + k_{ser,ax,\theta} cos\theta\left(cos\theta + \mu_f sin\theta\right) \qquad \text{Eq. 6}$$

where, $k_{ser,STS}$ is the SLS stiffness per screw under lateral load (N/mm); θ is the angle between timber grain and screw axis (rad); and μ_f is the friction coefficient.

(a) Washer in the steel plate

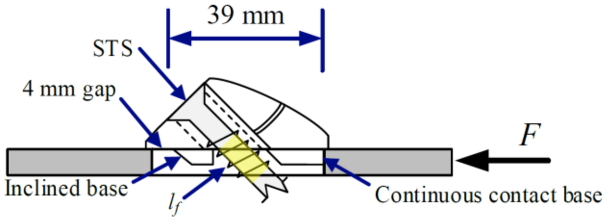

(b) Washer cross section view

Figure 8 Washer and STS details

To overcome the limitation of Eq. 6, Girhammar et al. [38] presented an analytical model for timber-to-timber connections that considers the effects of flexibility and extensibility of screws. Mirdad and Chui [39] proposed another analytical model for timber-concrete composite floors where a gap usually exists between timber and concrete. These two analytical models were combined in this paper to esimate $k_{ser,STS}$ as Eq. 7a, where the effective axial withdrawal stiffness per unit area K_{ax} (N/mm^3) and embedment stiffness per unit area K_h (N/mm^3) were based on STS withdrawal tests and embedment tests. Compared to tests in [39], the BRBGF tests used the same type of STS and similar density of timber (466 kg/m^3 vs. 419 kg/m^3 in [39]). Past research also showed that the density of the timber members had minor inpact on stiffness [30]. Thus, K_h = 6.52 N/mm^3 in [39] was used here. However, K_{ax} in [39] was only for 80 mm and 100 mm STS. Past research on screwed-in rods indicated that axial stiffness was disproportional to the penetration length [55]. Because of this, K_{ax} in [39] might not be suitable for 300 mm STS in the BRBGF tests. In this regard, STS withdrawal tests with different embedment length were conducted with three replicates for each penetration length as shown in Figure 9. Figure 9c shows the test results with the prediction curves of $k_{ser,ax,\theta,1}$ (Eq. 2) and $k_{ser,ax,\theta,2}$ (Eq. 3). It is illustrated that $k_{ser,ax,\theta,1}$ provided a conservative prediction while $k_{ser,ax,\theta,2}$ overestimated the axial stiffness considerably, which proved that $k_{ser,ax,\theta,2}$ was not suitable for long STS. Figure 9c also shows two power series models $k_{ser,ax,\theta,3}$ and $k_{ser,ax,\theta,4}$ based on the mean value (Eq. 8) and 5th-percentile value (Eq. 9) of test results calculated by EN 14358 [56], respectively. $k_{ser,ax,\theta,3}$ and $k_{ser,ax,\theta,4}$ can be used to estimate K_{ax} in modelling and design of the screwed connections, respectively. It should be noted that although $k_{ser,ax,\theta,1}$ provided conservative prediction, Blass et al [53] stated that $k_{ser,ax,\theta,1}$ was not applicable outside of their test series and should not be transferred to screws from other manufacturers. Therefore, it is recommended that screw manufacturers should conduct STS withdrawal tests and provide conservative stiffness equations in form of $k_{ser,ax,\theta,4}$ for their products in their ETA reports.

$$k_{ser,SLS} = \frac{3E_{STS}Id[2(3l_f + 2l_{ef})K_{ax,eq}\pi l_{ef}(cos^2\theta + 0.5\mu_f sin2\theta) + K_{h,eq}l_{ef}^2(sin^2\theta - 0.5\mu_f sin2\theta)]}{6E_{STS}I(3l_f + 2l_{ef}) + K_{h,eq}dl_{ef}^2 l_f^3 sin^2\theta} \qquad \text{Eq. 7a}$$

with:

$$K_{ax,eq} = K_{ax}\frac{\tanh(\omega l_{ef})}{\omega l_{ef}} \qquad \text{Eq. 7b}$$

$$K_{h,eq} = 2K_h \frac{sinh^2(\lambda l_{ef}) - sin^2(\lambda l_{ef})}{\omega l[\sinh(\lambda l_{ef})\cosh(\lambda l_{ef}) - \sin(\lambda l_{ef})\cos(\lambda l_{ef})]} \qquad \text{Eq. 7c}$$

$$\omega = 2\sqrt{K_{ax,eq}/E_{STS}d} \qquad \text{Eq. 7d}$$

$$\lambda = \sqrt[4]{K_h d/(E_{STS}I)} \qquad \text{Eq. 7e}$$

$$K_{ax} = \frac{k_{ser,ax,\theta}}{\pi l_{ef} d} \qquad \text{Eq. 7f}$$

$$K_h = \frac{k_{ser,lat,\theta}}{l_{ef} d} \qquad \text{Eq. 7g}$$

where, screw diameter d = 11 mm; elastic modulus of screw E_{STS} = 210 GPa; $I = \pi d^4/64$ (mm^4); The free length l_f = 12 mm; l_{ef} = (l_{em} - 10 mm) is the effective penetration length of STS (mm); l_{em} = 249 mm is the penetration length including the screw tip; $k_{ser,ax,\theta}$ and $k_{ser,lat,\theta}$ are the axial stiffness and lateral stiffness of STS with an angle of θ to the timber grain.

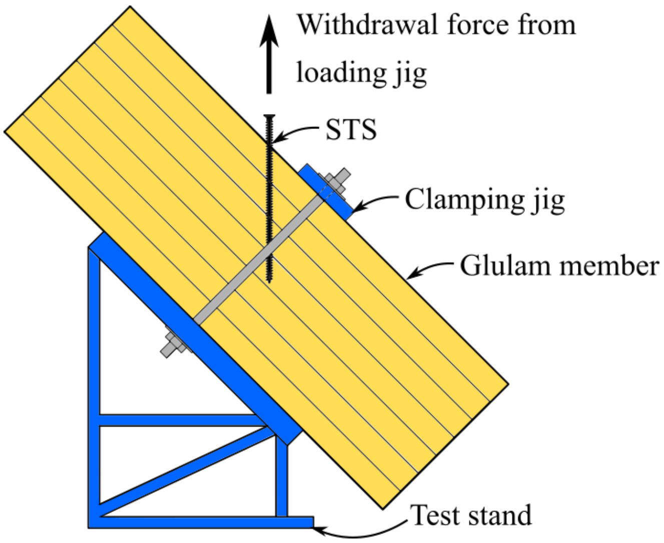

(a) Test side view

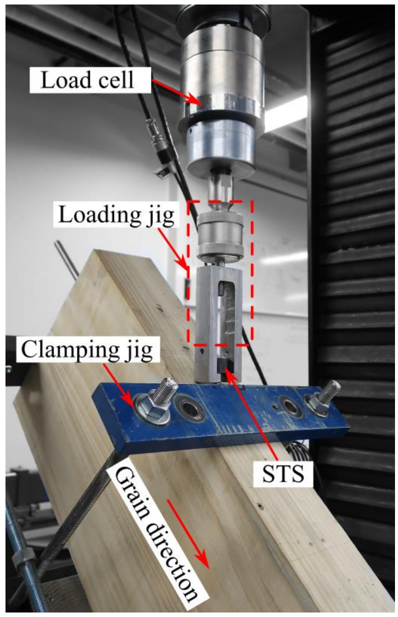

(b) Test setup

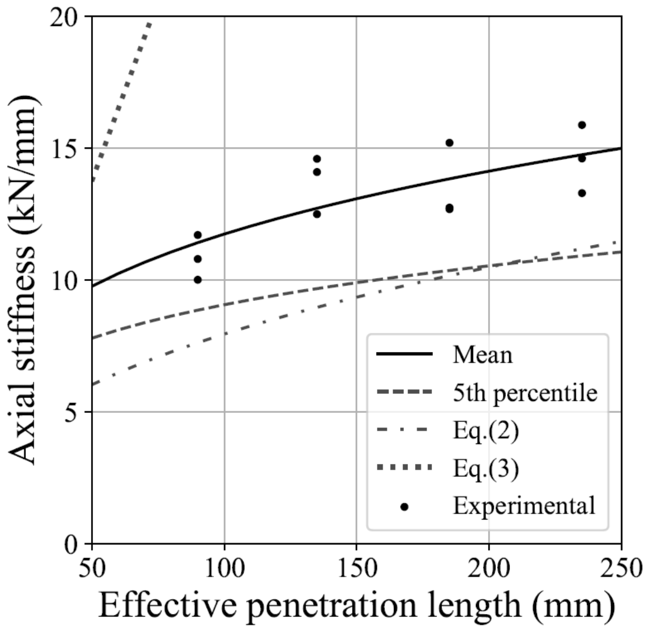

(c) Test results and curve fitting

Figure 9 STS withdrawal test

$$k_{ser,ax,\theta,3} = 3433 l_{ef}^{\ 0.267} \text{ for mean value (N/mm)} \qquad \text{Eq. 8}$$

$$k_{ser,ax,\theta,4} = 3321 l_{ef}^{\ 0.218} \text{ for 5th-percentile value (N/mm)} \qquad \text{Eq. 9}$$

Based on withdrawal tests, K_{ax}=1.81 N/mm^3 calculated by Eq. 7f and Eq. 8 was used to calculate the $k_{ser,SLS}$ in Eq. 7a. Table 3 shows that the analytical results underestimated the test results by 18% with friction coefficient μ_f=0.25 which was recommended by Krenn and Schickhofer [54] based on European practice. The reasons could be 1) μ_f is higher than 0.25 [38], for example μ_f=0.45 was reported by Mirdad and Chui [39]; 2) The assumption that withdrawal stresses along the length of the STS are evenly distributed is not appropriate. The part of STS deeply embeded into timber may engage less so the even distribution assumption underestimated the K_{ax} close to the timber surface. Because the analytical model provides reasonbly conservative prediction of the stiffness, it is used to model the screwed connection performance in the BRBGFs.

Table 3 Stiffness prediction comparison (kN/mm)

μ_f	Analytical model	Experimental*[9]	Difference (%)
0.25	303	371	-18
0.45	340	371	-8

*Note: this is for the screwed connection with 32 STS

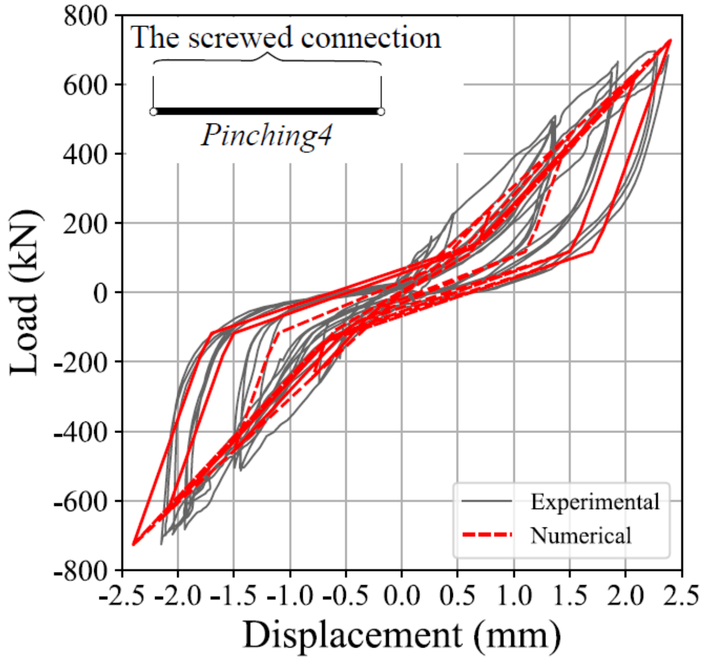

Figure 10 Comparison of the screwed connection

Because no damage of the screwed connections was observed in the BRBGF tests [9], the screwed connection loading stiffness was assumed to be constant. The stiffness prediction with μ_f=0.25 from the analytical model was input as the loading stiffness for the cyclic model simulated by *Pinching4* model in OpenSees. The reason for choosing μ_f as 0.25 was that it provided conservative predictions and was recommended by the European practice [54]. The unloading stiffness of the screwed connections was assumed as three times of their loading stiffness based on test observations to consider the loosening of STS under cyclic loading [9]. The parameters of *Pinching4* model for the screwed connections are also listed in Appendix I. Figure 10 shows the experimental and numerical results for the screwed connection. The results show that the model can be used to represent the performance of the screwed connections.

2.4 BRBGF model validation

The models of BRBGF specimens with the dowelled connections (S-D) and screwed connections (S-S) were established in the OpenSees as shown in Figure 11. The BRBGF tests by Dong et al. [9] showed that the dowelled connections and the screwed connections had limited moment-resisting capacity, so the beam-column connections were modelled as pinned connections. The BRB-timber interface connections were modelled by element 1-4 with two overlapped nodes. For each element, the translational stiffness, i.e. the horizontal and vertical connection stiffness, was modelled by the connection models introduced in Section 2.3, and the rotation stiffness was neglected due to the limited moment-resisting capacity of the connections. The initial slips of the top connection (element 1) and the bottom connections (element 2 and 3) were superposed together at the top connection and simulated by the *ElasticMultiLinear* material in OpenSees to simplify the models and improve the convergence of the models. Figure 12 illustrated that the model simulated hysteresis curves well. The difference between the experimental and numerical results was primarily from the BRB fit error shown in Figure 4 and the maximum force error of experimental tests in two loading directions. The accumulated energy dissipated by models was similar with the test results as shown in Figure 13. The difference was that the models dissipated slightly less energy in cycle No.8-No.11, which might be due to the higher unloading stiffness of BRBs in tests as mentioned before. The computational time with the loading protocol in Figure 12 and a displacement increment of 0.03 mm was 19.7 s for S-D model and 21.9 s for S-S model on a desktop with a Core i7-7700 processor and 16 GB RAM.

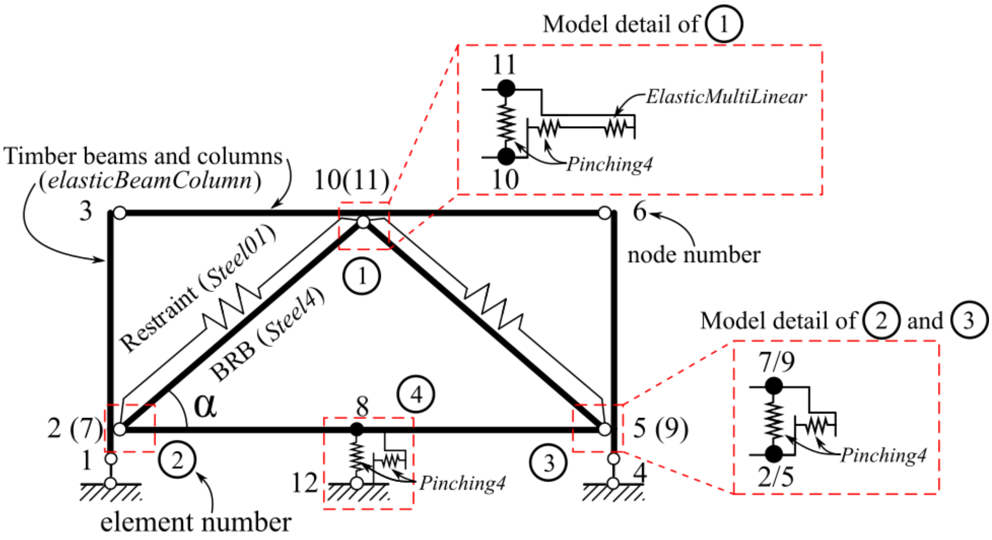

Figure 11 BRBGF model

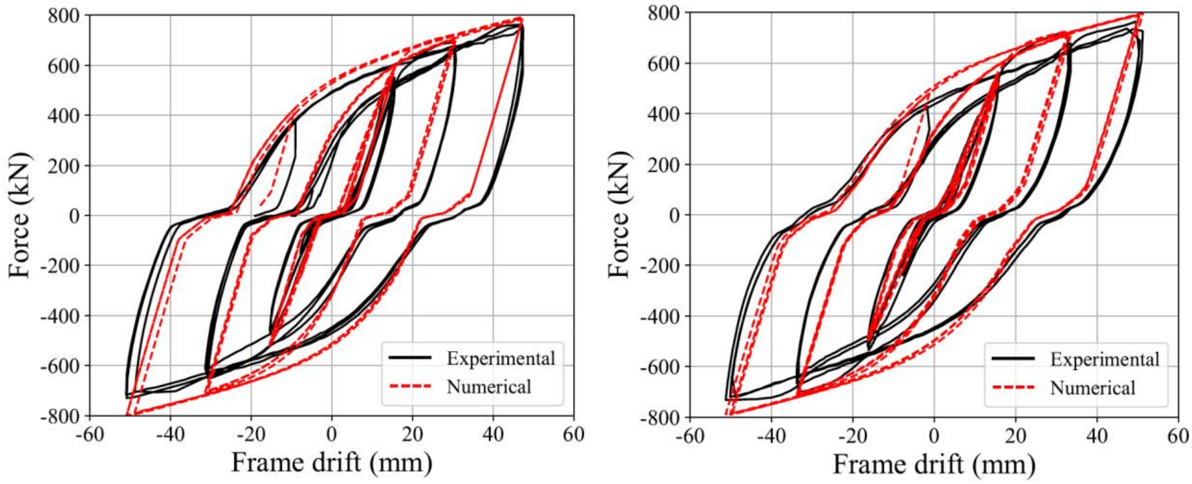

(a) S-D (Dowelled connections) (b) S-S (Screwed connections)

Figure 12 Comparison of BRBGF hysteresis curves

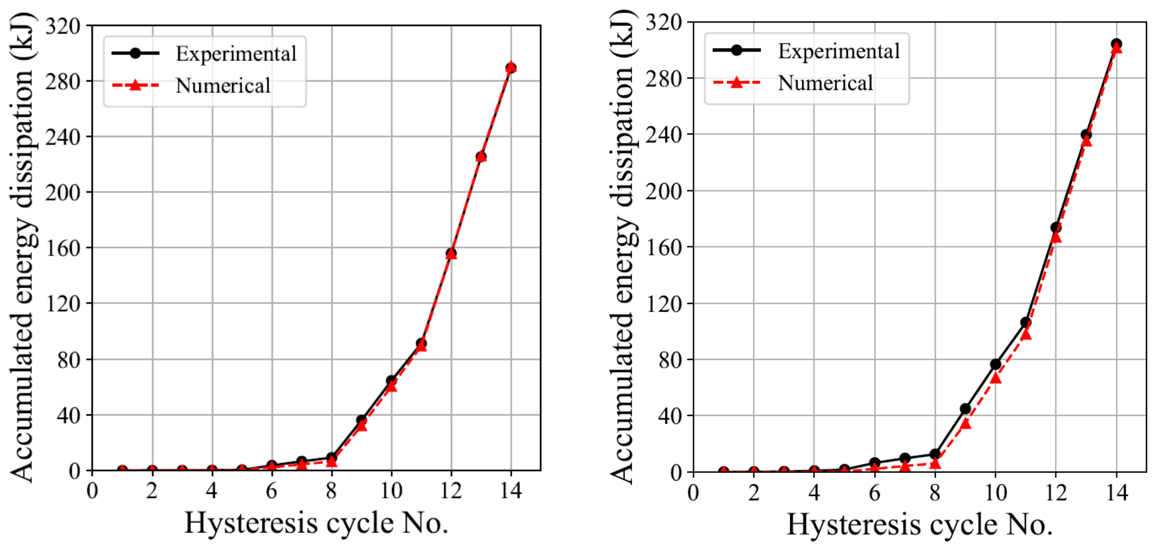

(a) S-D (Dowelled connections) (b) S-S (Screwed connections)

Figure 13 Comparison of BRBGF accumulated energy dissipations

Figure 14 and Figure 15 show BRB deformation versus frame drift for S-D and S-S, respectively. BRB-S and BRB-N represent the southern and northern BRB in Figure 1, respectively. The positive drift (toward north in Figure 1) causes elongation in the BRB-S and shortening in the BRB-N. At small drift levels, the BRB deformation in tests matched the simulation very well. At large drift levels, the BRB had greater elongation deformation than the shortening deformation, which was not captured by the model very well. This was likely because BRB in compression was restrained by concrete grout and had slightly higher stiffness than the BRB in tension. The different BRB deformation between S-D and S-S probably was caused by the variation of the yield location in tension. The yielding deformation might be concentrated on any location along the yield zone and the restraints around the location could be different. The strength difference of BRBGFs was also partially caused by the variation of restraints. Better quality construction of BRBs can reduce the uncertainty of restraints and help to achieve a more consistent performance.

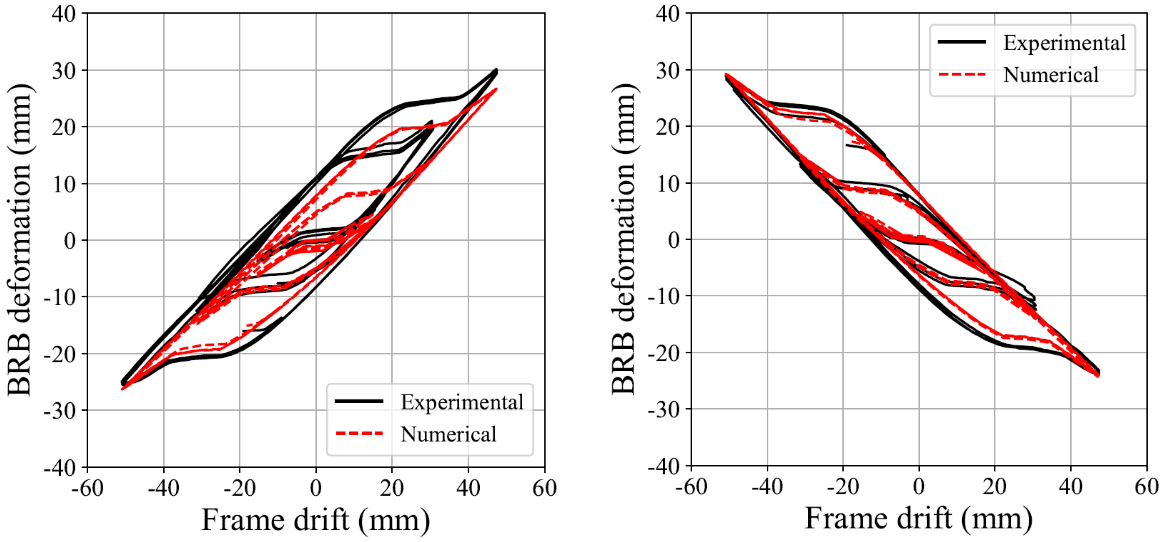

(a) BRB-S (b) BRB-N

Figure 14 Comparison of BRB deformation in S-D (Dowelled connections)

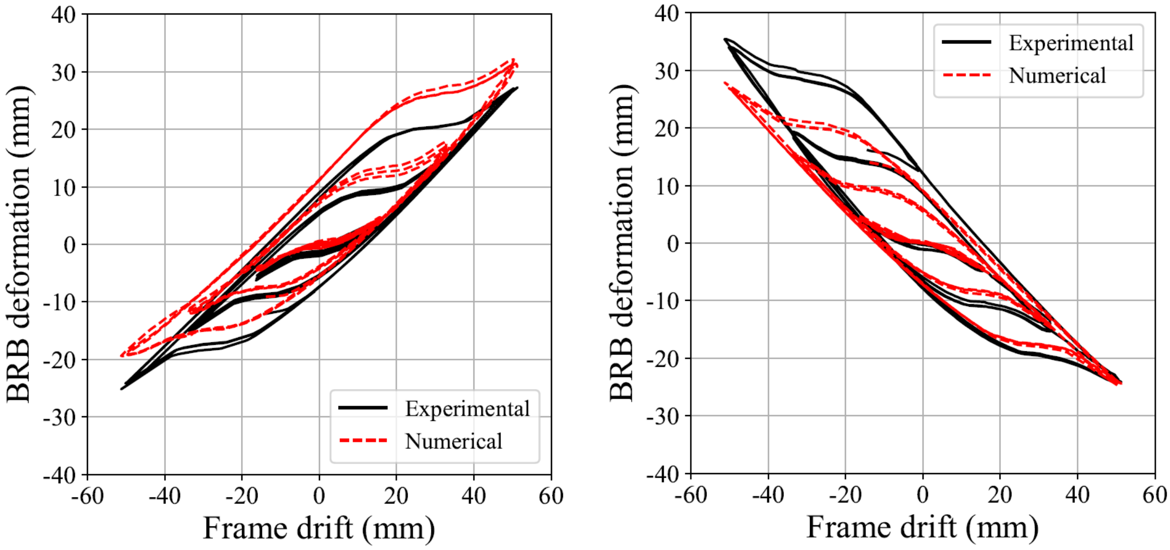

(a) BRB-S (b) BRB-N

Figure 15 Comparison of BRB deformation in S-S (Screwed connections)

To investigate the influence of the BRB-timber interface connections on the overall performance of the BRBGF, the *Pinching4* models in the S-S model were removed from Figure 11, so this new model only included the initial slips caused by the pin-end BRBs but the timber-steel interface connections were simulated to be translationally rigid. The hysteresis loops of the model with the rigid connections were compared with the S-S model in Figure 16. Figure 16 shows that the stiffness of the S-S model before BRBs' yielding was overestimated by 67% (65 kN/mm for the model rigid connections vs. 39 kN/mm for the S-S model). In addition, neglecting the increased slips due to the higher unloading stiffness of the timber connections will overestimate the energy dissipation. Therefore, it is important to include the connection models in the BRBGFs.

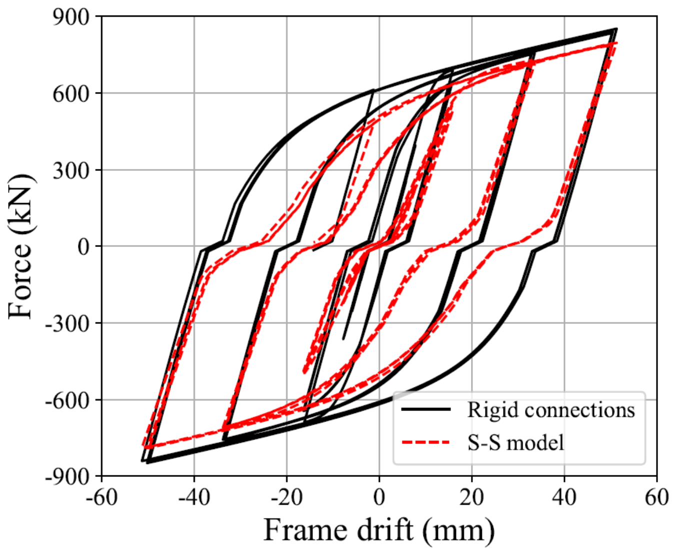

Figure 16 Comparison of the hysteresis curves with different connection modelling methods

3 Parametric studies

The validated one-bay one-storey BRBGF model in Figure 11 was used as a benchmark model for the parametric studies to investigate the influence of the critical BRB-timber interface connection details on the overall behaviour. The BRB restraint element shown in Figure 11 was removed from the model considering that the insufficient unbonding between the steel core and concrete grout was avoided by good quality construction of BRBs. The design overstrength factor of BRBs ($\gamma_{d,BRB} = \omega\beta$) is set as 1.5 at 2.0% drift ratio according to the BRB model analysis. This $\gamma_{d,BRB}$ is also typical of real BRBs [46].

3.1 Influence of interface connection stiffness

The stiffness of the BRB-timber interface connections could impact the efficiency of the BRBs. Unlike welded or bolted connections in steel frames, timber connections are more flexible. Eq. 10 defines the lateral stiffness ratio η between BRBGFs with translationally semi-rigid interface connections ($K_{in,\gamma}$) and translationally rigid interface connections ($K_{in,\infty}$, i.e. pinned connections). The connection overstrength factor γ in Eq. 11 is the ratio between the interface connection design strength R_d in Figure 2 and the lateral yield strength $F_{k,BRB}$ contributed by two BRB components.

$$\eta = K_{in,\gamma}/K_{in,\infty} \qquad \text{Eq. 10}$$

$$\gamma = R_d/F_{k,BRB} \qquad \text{Eq. 11}$$

$$F_{k,BRB} = 2\phi_m f_y A_c \cos\alpha \qquad \text{Eq. 12}$$

where, ϕ_m (= 1.25) is the material overstrength obtained from the coupon tests [9]; α is the inclined angle of BRBs as shown in Figure 11.

A series of BRBGF simulations were conducted. Here the same BRBs were used in all BRBGFs, so $F_{k,BRB}$ was assumed to remain constant, but γ was increased from 1.0 to 2.5. The increase in γ implied a greater number of dowels and screws in the connections. This increased connection stiffness and stiffness ratio η. The relationships between η and γ for S-D and S-S frames are shown in Figure 17. It was found that η was increased by 19% (from 0.75 to 0.89) and 38% (from 0.58 to 0.80) for S-D and S-S, respectively, when γ was increased from 1.0 to 2.5. However, increasing γ did not improve η proportionally and might significantly increase the fastener number of connections. For example, by increasing γ from 1.5 to 2.5 by 67%, meaning the interface connections were significantly stronger, η was increased by only 9% (from 0.82 to 0.89). For S-S, η was increased by 18% when γ was increased from 1.5 to 2.5, slightly more efficient than S-D. Figure 18 shows the pushover curves of S-D with different γ. It was illustrated by Figure 18 that when the capacity design was not achieved ($\gamma < 1.5$). In this case, the connections were designed to be weaker than the expected maximum strength of BRBs considering their overstrength at 2% drift ratio. Inelastic deformation in the connections could occur and the system stiffness was lower than the case when capacity design would be achieved (γ = 1.5 and γ = 2.5). Therefore, it is important to keep γ equal to or even exceed the BRB overstrength factor $\gamma_{d,BRB}$ to maximize the efficiency of BRBs and avoid significant inelastic response or damage of the connections. When γ was over $\gamma_{d,BRB}$ (γ = 1.5 and γ = 2.5), the stiffness difference was relatively small. For a more cost-effective connection design, γ = 1.5 is recommended for both connections. Because this is the minimum value (i.e. $\gamma = \gamma_{d,BRB}$) to ensure the achievement of the capacity design and the connections also have enough stiffness to engage BRBs.

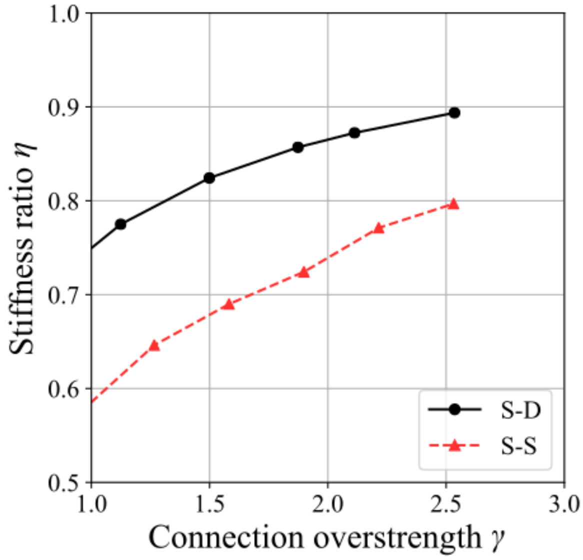

Figure 17 The relationship between stiffness ratio and connection overstrength

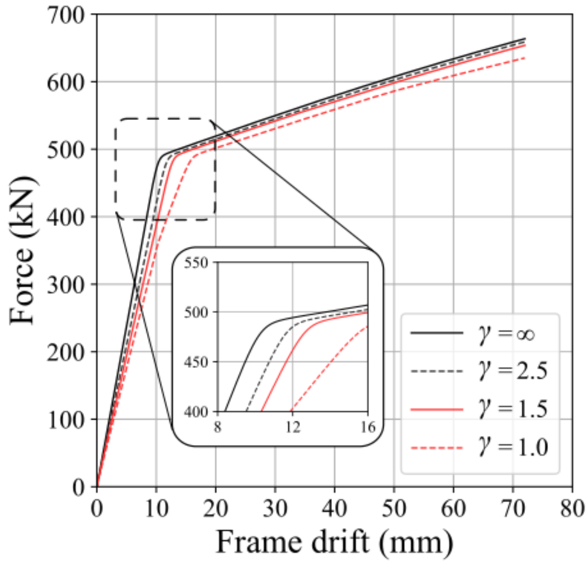

Figure 18 Pushover curves of S-D with different connection overstrength

Figure 18 also shows that the ultimate strength at 2.0% drift ratio is 654 kN for $\gamma = 1.5$ and 659 kN for $\gamma = 2.5$ with less than 1% increase. The post-yield stiffness is similar among different γ because it is controlled by the stiffness of BRBs. As a result, when γ is over $\gamma_{d,BRB}$, the connection stiffness only had a small impact on the initial stiffness, but a negligible effect on the ultimate strength and post-yield stiffness. Lower initial stiffness could increase the yield displacement and SLS might become the governing case for the system design.

3.2 Influence of manufacturing tolerances

The pin-end connections of BRBs to the gusset plates require tolerances for installation as well as the dowelled connections in S-D. The slack caused by the tolerances may reduce the system's energy dissipation under cyclic loading [57]. Therefore, the influence of manufacturing tolerances on the cyclic performance of the BRBGFs was investigated.

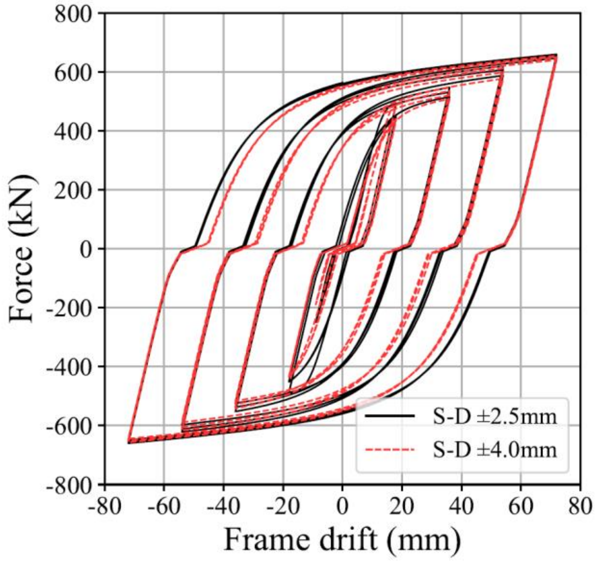

Figure 19 Hysteresis curves with different initial slips

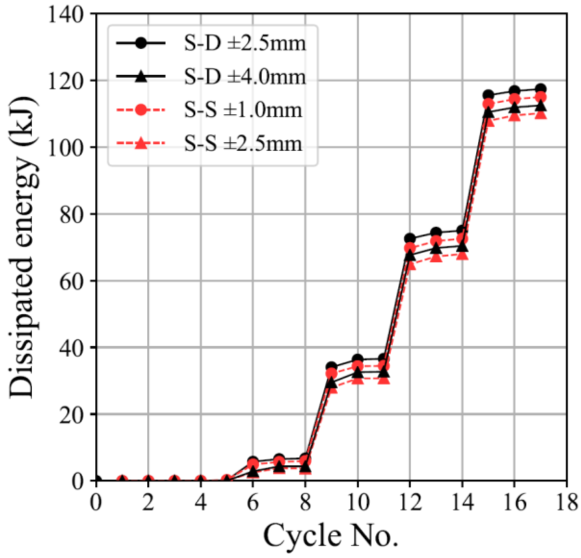

Figure 20 Energy dissipation per cycle of BRBGFs

The tolerances in the pin and dowel holes can cause initial slips of the system, so BRBGFs with different initial slips were modelled to study the influence of manufacturing tolerances. All connections were designed by the same connection overstrength factor γ (= 1.5). The benchmark BRBGF model contained two BRBs and three connections as shown in Figure 11. Each BRB allows 1 mm tolerance in total from pin holes on both ends [44], which can cause a ±0.5 mm initial slip in the system. Similarly, each dowelled connection can have minimum 1 mm and maximum 2 mm tolerances [23], i.e. ±0.5 mm and ±1.0 mm initial slips. Therefore, the upper limit of initial slips for the S-D model was assumed as ±4.0 mm (there were two BRBs in the S-D model and the initial slip was ± 0.5 mm from each BRB, i.e. ± 0.5 × 2; while there was one top connection and two bottom connections in the S-D model and the initial slip was ± 1.0 mm from each connection as the maximum, i.e. ± 1.0 mm × 3. The upper limit initial slip was ±0.5 mm × 2 plus ±1.0 mm × 3) and the lower limit was assumed as ±2.5 mm (± 0.5 mm × 2 from the BRBs plus ±0.5 mm × 3 from the connections). The screwed connections can be tight fit while a maximum 1 mm tolerance is considered conservatively to fully engage all STS. For S-S, the upper and lower limits were ± 2.5 mm (±0.5 mm×2 from the BRBs plus ± 0.5 mm × 3 from the connections) and ±1.0 mm (±0.5 mm×2 from the BRBs plus ±0.0 mm×3 from the connections), respectively.

Figure 19 shows the hysteresis loops of S-D following the loading protocol in the experimental tests [9] as an example. It is shown that S-D with ±2.5 mm initial slips started to carry the load 1.5 mm earlier than S-D with ±4.0 mm initial slips before yielding and when the load direction changed. However, they tended to be consistent at post-yielding stage. Figure 20 shows the energy dissipation in each cycle of S-D and S-S. The results show that hysteresis loops with different initial slips were similar and the maximum difference of energy dissipations in one cycle is within 5% (117 kJ for "S-D ±2.5 mm" vs. 112 kJ for "S-D ±4.0 mm" and 115kJ for "S-S ±1.0 mm" vs. 110 kJ for "S-S ±2.5 mm" in cycle No. 17). Therefore, the initial slips from manufacturing tolerances increase the yield displacement. A higher displacement before yielding is expected with larger manufacturing tolerances and SLS may become the governing case for the system design. The manufacturing tolerances have a negligible impact on the ultimate strength and energy dissipation of BRBGFs.

4 Conclusions

This paper presented a component-based numerical model in OpenSees to simulate the cyclic behaviour of BRBGFs. Special intent was the stiffness of the BRB-timber interface connections and the manufacturing tolerances as well as their effects on the BRBGF performance. The main conclusions are drawn as follows:

(1) The beam-on-foundation (BOF) model provided more accurate stiffness predictions of the dowelled connections compared with the stiffness equation in Eurocode 5. The combined analytical model from literature was able to predict the stiffness of the screwed connections with reasonable accuracy. It is suggested to build databases of the standard embedment tests for dowels and different timber species, so the stiffness for dowelled connections can be predicted by the BOF model and the stiffness equations in Eurocode 5 can be improved. More withdrawal tests of screws are also suggested to be conducted by the screw suppliers for the improved stiffness predictions.

(2) The BRBGF model predictions agreed well with the experimental results of two full-scale BRBGFs in terms of force-drift responses, accumulated energy dissipation and BRB deformations.

(3) The dowelled connections and screwed connections as the BRB-timber interface connections effectively engaged the BRBs. The parametric studies showed that when connection overstrength factor γ was 1.5, the stiffness of BRBGFs with the dowelled and the screwed connections achieved 82% and 68% of the stiffness of BRBGFs with translationally rigid BRB-timber connections (pinned connections), respectively. Further increasing the connection strength did not increase the system lateral stiffness significantly.

(4) The manufacturing tolerances can cause initial slips of BRBGFs. The parametric studies showed that the practical manufacturing tolerances did not affect the energy dissipation and ultimate strength of the BRBGFs significantly under cyclic loading. However, excessive initial slips could cause more system drifts before the yielding of BRBs, and might affect the serviceability performance. The manufacturing tolerances should be decided by design engineers according to the serviceability loads and drift limit of non-structural elements in a project.

5 Acknowledgements

The authors would like to acknowledge Natural Hazards Research Platform, QuakeCore, University of Canterbury, and Shanghai Research Institute of Materials for sponsoring the project. The authors would also like to acknowledge the helps from lab technicians Russell McConchie, Alan Thirlwell, Michael Weavers, Peter Coursey and Dave Carney during the tests and Prof. Timothy Sullivan, Assoc. Prof. Charles Clifton, Dr. Ádám Zsarnóczay, and Ben Sitler when preparing the manuscript.

Appendix I: Parameters for the numerical models in OpenSees

The parameters for the *Steel4* in Section 2.2 are listed in the Table A1. The parameters were calibrated by Zsarnóczay and Vigh [47] and the detailed information of the model and parameters can be found in the OpenSees documentation [40].

Table A1 Parameters for *Steel4*

Parameters	Tension	Compression
Steel properties	Steel core area A_c (mm^2) = 1120 Modulus of elasticity (MOE) E_s (MPa) =210000	
f_{sm}	1.22	
Equivalent MOE E_{eq} (MPa)	$E_s f_{sm}$=256200	
Yield strength f_y (MPa)	294	
Ultimate strength f_u (MPa)	1.65f_y=485	2.5f_y=735
Hardening ratio b_k	0.4%	2.5%
R_0	25.0	
r_1	0.91	

r_2	0.15	
R_u	2.0	
b_i	0.08%	
b_l	$0.06+0.02\times600/A_y$=0.07%	
ρ_i	$1.15+0.45\times600/A_y$=1.39	$0.85+0.25(600/A_y)^{0.5}$=1.03
R_i	3.0	
l_{yp}	1.0	

The dowelled connections in Section 2.3.1 was simulated by *Pinching4* and *Elastic MultiLinear* models in the OpenSees. The parameters of the top connection are listed in Table A2. The bottom connections were assumed to be half the strength of the top connections because the load level for the bottom connections wasapproximately half the top connections. The meaning of parameters can be found in Figure A1 and the OpenSees documentation [40]. The parameters for the negative curve (for example, eNd_1 and eNf_1) were chosen to be the same with those for the positive curve.

Table A2 *Pinching4* and *ElasticMultiLinear* parameters for the dowelled connection

Material	Parameters
Pinching4	ePd_1 = 0.01 mm, ePf_1 = 12028 N; ePd_2 = 0.7 mm, ePf_2 = 421008 N; ePd_3 = 2.0 mm; ePf_3 = 774948 N; ePd_4 = 3.4 mm. ePf_4 = 962000 N; r_{DsipP} = 0.0, r_{ForceP} = 0.0, u_{ForceP} = -0.05; $g_{Klim} = g_{Dlim} = g_{Flim} = g_E$ = 0.0;
ElasticMultiLinear	-strain: [-2.0 -0.5 0.0 0.5 2.0] (mm) -stress: [-50000000 -8000 0 8000 5000000] (N)

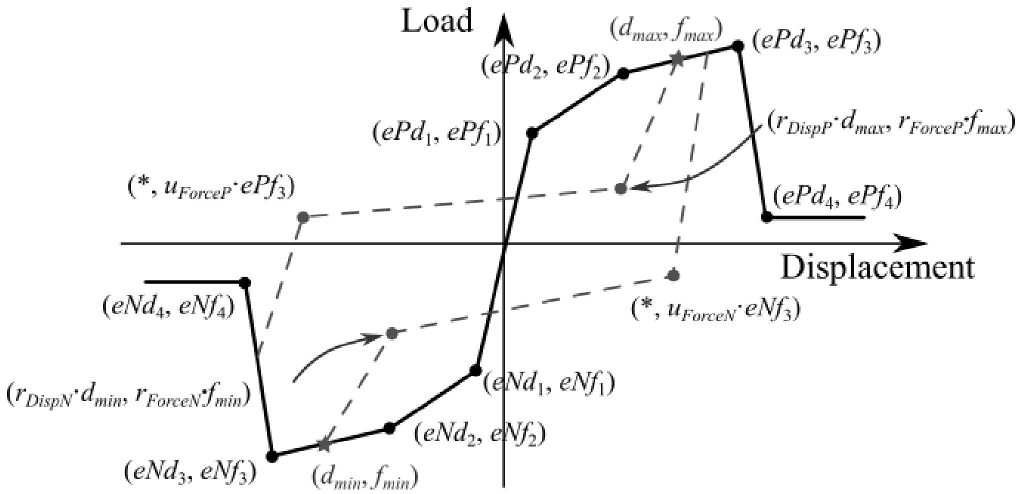

Figure A1 *Pinching4* model in the OpenSees

The screwed connections in Section 2.3.2 was simulated by *Pinching4* model in the OpenSees. The parameters of the top connection are listed in Table A3. The bottom connections were assumed to be half the strength of the top connections as well. The parameters for the negative curve (for example, eNd_1 and eNf_1) were chosen to be the same with those for the positive curve.

Table A3 *Pinching4* parameters for the screwed connection

Material	Parameters
Pinching4	ePd_1 = 0.01 mm, ePf_1 = 9090 N; ePd_2 = 2.0 mm, ePf_2 = 606000 N; ePd_3 = 4.0 mm; ePf_3 = 1212000 N; ePd_4 = 10.0 mm. ePf_4 = 1333200 N; r_{DsipP} = 0.3, r_{ForceP} = 0.2, u_{ForceP} = -0.1;
	$g_{Klim} = g_{Dlim} = g_{Flim} = g_E$ = 0.0;

6 References

[1] Sun X, He M, Li Z. Novel engineered wood and bamboo composites for structural applications: State-of-art of manufacturing technology and mechanical performance evaluation. Constr Build Mater 2020;249:118751. https://doi.org/10.1016/j.conbuildmat.2020.118751.

[2] Lam F, Gehloff M, Closen M. Moment-resisting bolted timber connections. Proc Inst Civ Eng Struct Build 2010;163:267–74. https://doi.org/10.1680/stbu.2010.163.4.267.

[3] Jia L-J, Dong Y, Ge H, Kondo K, Xiang P. Experimental study on high-performance buckling-restrained braces with perforated core plates. Int J Struct Stab Dyn 2019;19:1940004.

[4] Shao F, Gu T, Jia LJ, Ge H, Taguchi M. Experimental study on damage detectable brace-type shear fuses. Eng Struct 2020;225:111260. https://doi.org/10.1016/j.engstruct.2020.111260.

[5] Popovski M. Seismic performance of braced timber frames. University of British Columbia, 2000.

[6] Kirstein A, Siracusa J, Smith T. The new timber von Haast replacement building in Christchurch. 2018 NZSEE Conf 2018:1–9.

[7] Li Z, Wang X, He M. Experimental and Analytical Investigations into Lateral Performance of Cross-Laminated Timber (CLT) Shear Walls with Different Construction Methods. J Earthq Eng 2020. https://doi.org/10.1080/13632469.2020.1815609.

[8] Li Z, Chen F, He M, Zhou R, Cui Y, Sun Y, et al. Lateral Performance of Self-Centering Steel–Timber Hybrid Shear Walls with Slip-Friction Dampers: Experimental Investigation and Numerical Simulation. J Struct Eng 2021;147:04020291. https://doi.org/10.1061/(asce)st.1943-541x.0002850.

[9] Dong W, Li M, Lee C, Macrae G, Abu A. Experimental testing of full-scale glulam frames with buckling restrained braces. Eng Struct 2020;222:111081. https://doi.org/10.1016/j.engstruct.2020.111081.

[10] Yu YJ, Tsai KC, Li CH, Weng YT, Tsai CY. Analytical simulations for shaking table tests of a full scale buckling restrained braced frame. Procedia Eng 2011;14:2941–8. https://doi.org/10.1016/j.proeng.2011.07.370.

[11] Guerrero H, Ji T, Teran-Gilmore A, Escobar JA. A method for preliminary seismic design and assessment of low-rise structures protected with buckling-restrained braces. Eng Struct 2016;123:141–54. https://doi.org/10.1016/j.engstruct.2016.05.015.

[12] Black CJ, Makris N, Aiken ID. Component testing, seismic evaluation and characterization of buckling-restrained braces. J Struct Eng 2004;130:880–94.

[13] Vigh LG, Zsarnóczay Á, Balogh T. Eurocode conforming design of BRBF – Part I: Proposal for codification. J Constr Steel Res 2017;135:265–76. https://doi.org/10.1016/j.jcsr.2017.04.010.

[14] Naghavi M, Rahnavard R, Thomas RJ, Malekinejad M. Numerical evaluation of the hysteretic behavior of concentrically braced frames and buckling restrained brace frame systems. J Build Eng 2019;22:415–28. https://doi.org/10.1016/j.jobe.2018.12.023.

[15] Zona A, Dall'Asta A. Elastoplastic model for steel buckling-restrained braces. J Constr Steel Res 2012;68:118–25. https://doi.org/10.1016/j.jcsr.2011.07.017.

[16] Sabelli R, Mahin S, Chang C. Seismic demands on steel braced frame buildings with buckling-restrained braces. Eng Struct 2003;25:655–66. https://doi.org/10.1016/S0141-0296(02)00175-X.

[17] Rahnavard R, Naghavi M, Aboudi M, Suleiman M. Investigating modeling approaches of buckling-restrained braces under cyclic loads. Case Stud Constr Mater 2018;8:476–88. https://doi.org/10.1016/j.cscm.2018.04.002.

[18] Atlayan O, Charney FA. Hybrid buckling-restrained braced frames. J Constr Steel Res 2014;96:95–105. https://doi.org/10.1016/j.jcsr.2014.01.001.

[19] Qu Z, Kishiki S, Maida Y, Sakata H, Wada A. Seismic responses of reinforced concrete frames with buckling restrained braces in zigzag configuration. Eng Struct 2015;105:12–21. https://doi.org/10.1016/j.engstruct.2015.09.038.

[20] Tsai CY, Tsai KC, Chen LW, Wu AC. Seismic performance analysis of BRBs and gussets in a full-scale 2-story BRB-RCF specimen. Earthq Eng Struct Dyn 2018;47:2366–89. https://doi.org/10.1002/eqe.3073.

[21] Blomgren H-E, Koppitz J-P, Valdés AD, Ko E. The heavy timber buckling-restrained braced frame as a solution for commercial buildings in regions of high seismicity. World Conf. Timber Eng., Vienna, Austria: 2016.

[22] Timmers M, Tsay Jacobs A. Concrete apartment tower in Los Angeles reimagined in mass timber. Eng Struct 2018;167:716–24. https://doi.org/10.1016/j.engstruct.2017.11.047.

[23] British Standard Institution (BSI). Eurocode 5: design of timber structures—Part 1-1: General—Common rules and rules for buildings 2004.

[24] Sawata K, Yasumura M. Estimation of yield and ultimate strengths of bolted timber joints by nonlinear analysis and yield theory. J Wood Sci 2003;49:383–91. https://doi.org/10.1007/s10086-002-0497-3.

[25] Gattesco N, Toffolo I. Experimental study on multiple-bolt steel-to-timber tension joints. Mater Struct Constr 2004;37:129–38. https://doi.org/10.1617/13724.

[26] Sawata K, Sasaki T, Kanetaka S. Estimation of shear strength of dowel-type timber connections with multiple slotted-in steel plates by European yield theory. J Wood Sci 2006;52:496–502. https://doi.org/10.1007/s10086-006-0800-9.

[27] Sandhaas C, van de Kuilen JWG. Strength and stiffness of timber joints with very high strength steel dowels. Eng Struct 2017;131:394–404. https://doi.org/10.1016/j.engstruct.2016.10.046.

[28] Jorissen AJM. Double shear timber connections with dowel type fasteners. Delft University Press Delft, The Netherlands, 1998.

[29] Wang C, Lyu J, Zhao J, Yang H. Experimental investigation of the shear characteristics of steel-to-timber composite joints with inclined self-tapping screws. Eng Struct 2020;215:110683. https://doi.org/10.1016/j.engstruct.2020.110683.

[30] Jockwer R, Jorissen A. Stiffness and deformation of connections with dowel-type fasteners. Des Connect Timber Struct 2018:95.

[31] Lemaître R, Epinal F, Bocquet J-F, Schweigler M, Bader TK. Beam-on-foundation modelling as an alternative design method for single fastener connections. Des Connect Timber Struct 2018:207.

[32] Lemaitre R, Bocquet J-F, Schweigler M, Bader TK. Beam-on-Foundation Modelling as an Alternative Design Method for Timber Joints with Dowel-Type Fasteners–Part 2: Modelling Techniques for Multiple Fastener Connections. 6th INTER Proceedings, 2019 Int. Netw. Timber Eng. Res. 2019, Tacoma, USA, Karlsruher Inst. für Technol. 2019, 2019.

[33] Approval ET. European Technical Approval ETA-11 / 0190 2016.

[34] ETA(European Technical Assessment). RothoBlaas Self-tapping screws and threaded rods ETA-11 / 0030 of 2019-10-08. 2019.

[35] Ringhofer A. Axially Loaded Self-Tapping Screws in Solid Timber and Laminated Timber Products. Verlag der Technischren Universität Graz; 2017. https://doi.org/10.3217/978-3-85125-555-3.

[36] Dietsch P, Brandner R. Self-tapping screws and threaded rods as reinforcement for structural timber elements-A state-of-the-art report. Constr Build Mater 2015;97:78–89. https://doi.org/10.1016/j.conbuildmat.2015.04.028.

[37] Tomasi R, Crosatti A, Piazza M. Theoretical and experimental analysis of timber-to-timber joints connected with inclined screws. Constr Build Mater 2010;24:1560–71.

https://doi.org/10.1016/j.conbuildmat.2010.03.007.

[38] Girhammar UA, Jacquier N, Källsner B. Stiffness model for inclined screws in shear-tension mode in timber-to-timber joints. Eng Struct 2017;136:580–95. https://doi.org/10.1016/j.engstruct.2017.01.022.

[39] Mirdad MAH, Chui YH. Stiffness prediction of Mass Timber Panel-Concrete (MTPC) composite connection with inclined screws and a gap. Eng Struct 2020;207:110215. https://doi.org/10.1016/j.engstruct.2020.110215.

[40] Mazzoni S, McKenna F, Scott MH, Fenves GL. OpenSees command language manual. Pacific Earthq Eng Res Cent 2006;264.

[41] American Institute of Steel Construction (AISC). Seismic provisions for structural steel buildings. ANSI/AISC 341-16. Chicago, IL: 2016.

[42] New Zealand Standards. NZS3603:1993 Timber structures standard 1993.

[43] Chinese Global Standards. GB50017-2017: Code for Design of Steel Structures. Beijing, China: China Architecture & Building Press Beijing, China; 2017.

[44] New Zealand Standards. NZS 3404: Part 1:1997 - Steel Structure Standard. Wellington, New Zealand: New Zealand Standards; 1997.

[45] Rothoblaas. VGU: 45° washer for VGS - Bright zinc plated carbon steel. 2017.

[46] Zsarnóczay Á. Experimental and numerical investigation of buckling restrained braced frames for Eurocode conform design procedure development. Budapest University of Technology and Economics, 2013.

[47] Zsarnóczay Á, Vigh LG. Eurocode conforming design of BRBF – Part II: Design procedure evaluation. J Constr Steel Res 2017;135:253–64. https://doi.org/10.1016/j.jcsr.2017.04.013.

[48] Sitler B, Takeuchi T. Higher-mode buckling and friction in long and large-scale buckling-restrained braces. Struct Des Tall Spec Build 2021;30:e1812.

[49] Jones AS. Design and sensitivity of buckling restrained braces. University of Canterbury, 2020.

[50] Hosford WF. Mechanical behavior of materials 2005;9780521846. https://doi.org/10.1017/CBO9780511810930.

[51] ASTM standard. ASTM D5764: Standard Test Method for Evaluating Dowel-Bearing Strength of Wood and Wood-. vol. 03. 2002. https://doi.org/10.1520/D5764-97AR13.2.

[52] Dorn M. Investigations on the Serviceability Limit State of Dowel-Type Timber Connections. Vienna University of Technology, 2012.

[53] Blaß HJ, Bejtka I, Uibel T. Tragfähigkeit von Verbindungen mit selbstbohrenden Holzschrauben mit Vollgewinde. KIT Scientific Publishing; 2006.

[54] Krenn H, Schickhofer G. Joints with inclined Screws and Steel Plates as outer Members. Proc. Int. Counc. Res. Innov. Build. Constr. Work. Comm. W18 – timber Struct. Meet. 42, Duebendorf, Switzerland: 2009.

[55] Blaß HJ, Krüger O. Schubverstärkung von Holz mit Holzschrauben und Gewindestangen. Band 15 der Reihe Karlsruher Berichte zum Ingenieurholzbau 2010.

[56] (BSI) BSI. 14358: 2016, Timber structures–Calculation and verification of characteristic values 2016.

[57] Wijanto S, Clifton GC. Experimental testing and design of BRB with bolted and pinned connections. Bull New Zeal Soc Earthq Eng 2014;47:264–74.

https://doi.org/10.5459/bnzsee.47.4.264-274.